RSC Advances

PAPER

View Article Online
View Journal | View Issue

Cite this: *RSC Adv.*, 2024, **14**, 22393

Conformational transitions in redissolved silk fibroin films and application for printable self-powered multistate resistive memory biomaterials†

Valeria Libera,[a] Rocco Malaspina,[a] Silvia Bittolo Bon,[a] Martina Alunni Cardinali,[b] Irene Chiesa,[c] Carmelo De Maria,[c] Alessandro Paciaroni,[a] Caterina Petrillo,[a] Lucia Comez,[d] Paola Sassi[b] and Luca Valentini[*e]

3D printing of water stable proteins with elastic properties offers a broad range of applications including self-powered biomedical devices driven by piezoelectric biomaterials. Here, we present a study on water-soluble silk fibroin (SF) films. These films were prepared by mixing degummed silk fibers and calcium chloride ($CaCl_2$) in formic acid, resulting in a silk I-like conformation, which was then converted into silk II by redissolving in phosphate buffer (PBS). Circular dichroism, Raman and infrared (IR) spectroscopies were used to investigate the transitions of secondary structure in silk I and silk II as the pH of the solvent and the sonication time were changed. We showed that a solvent with low pH (*e.g.* 4) maintains the silk I β-turn structure; in contrast solvent with higher pH (*e.g.* 7.4) promotes β-sheet features of silk II. Ultrasonic treatment facilitates the transition to water stable silk II only for the SF redissolved in PBS. SF from pH 7.4 solution has been printed using extrusion-based 3D printing. A self-powered memristor was realized, comprising an SF-based electric generator and an SF 3D-printed memristive unit connected in series. By exploiting the piezoelectric properties of silk II with higher β-sheet content and Ca^{2+} ion transport phenomena, the application of an input voltage driven by a SF generator to SF 3D printed holey structures induces a variation from an initial low resistance state (LRS) to a high resistance state (HRS) that recovers in a few minutes, mimicking the transient memory, also known as short-term memory. Thanks to this holistic approach, these findings can contribute to the development of self-powered neuromorphic networks based on biomaterials with memory capabilities.

Received 16th April 2024
Accepted 9th July 2024

DOI: 10.1039/d4ra02830a

rsc.li/rsc-advances

Introduction

Ionic conductors are frequently employed to design bioelectronics for mimicking life systems.[1–3] The human brain is an excellent example where the stimulation triggers ion transport across cell membranes enabling the transmission and storing of information.[4–8] The pillars of this intricate transmission network are the neurons that communicate through synapses.[9] The synapses use chemical mediators (*e.g.*, Ca^+, Na^+, and K^+) from presynaptic to postsynaptic terminals.[10] The earliest studies indicated that the ion/electron coupling is the secret of electrophysiological experiments.[11] An increasing investigation interest is thus dedicated to materials that couple ion/electron interfaces and ion conductivity for logic circuits. Inspired by natural silk spinning, redissolved (regenerated) silk fibroin (SF) is an ionotronic biomaterial consisting of three elements: protein, metal ions (calcium chloride), and water. SF protein provides the biocompatibility, biodegradation and mechanical properties similar to those of soft tissues; metal ions are responsible of ionic conductivity and, finally, water is indispensable for ion mobility.[12–14]

Regenerated SF is normally stabilized in the silk II conformation by inducing β-sheet formation through solvents[15] or by physical stretching.[16] For example, SF films prepared by the dissolution in formic acid (FA) with the addition of calcium chloride ($CaCl_2$) exhibit the silk I secondary structure, which rapidly dissolves in water compared with methanol-treated films with a high crystalline fraction.[17] Moreover, Yucel *et al.*[18] associated the piezoelectricity of SF with the crystalline fraction of its structure consisting of a light chain (L-chain) and heavy chain (H-chain)

[a]*Dipartimento di Fisica e Geologia, Università degli Studi di Perugia, Via A. Pascoli, 06123, Perugia, Italy*
[b]*Department of Chemistry, Biology and Biotechnology, University of Perugia, Via Elce di Sotto 8, 06123, Perugia, Italy*
[c]*Department of Ingegneria dell'Informazione, Research Center E. Piaggio, University of Pisa, Largo Lucio Lazzarino 1, Pisa, 56122, Italy*
[d]*CNR-IOM – Istituto Officina dei Materiali, National Research Council of Italy, Via Alessandro Pascoli, 06123 Perugia, Italy*
[e]*Civil and Environmental Engineering Department, INSTM Research Unit, University of Perugia, Strada di Pentima 8, 05100, Terni, Italy. E-mail: luca.valentini@unipg.it*

† Electronic supplementary information (ESI) available: Fig. S1: Optical image and Raman spectrum of the holey structures fabricated *via* extrusion-based 3D printing of SF solution in PBS on ITO after the analysis presented in Fig. 5. Fig. S2: Current fluctuation from cycle 1 to cycle 5 of Fig. 5b. See DOI: https://doi.org/10.1039/d4ra02830a

polypeptide. SF's piezoelectric capabilities were attributed to the presence of the H-chain hydrophobic domains that organize themselves into β-sheets, which is the primary source of silk's piezoelectricity. In recent years, several studies have reported piezoelectricity in SF composites by combining SF with gold nanorods and carbon nanotubes.[19–21] It was found also the tribo-electrical properties by changing the electric field distribution of the SF film with mechanical pressure when interfaced with poly(3-hydroxybutyrate-*co*-3-hydroxyvalerate) (PHBV).[19] SF loaded with carbon nanotubes was used to fabricate a 3D printable bio-adhesive ink for self-powered applications.[21] However, enhancing the intrinsic piezoelectricity of SF is correlated to the β-sheet secondary structures by adjusting the processing parameters.

On the contrary, the high solubility, low viscosity and good wettability on specific substrates of SF with a high silk I content (hydrated β-turn crystal structure)[22] enable its printability using extrusion-based printing (EBP).

Despite the critical role of the silk I and silk II secondary conformation on the material properties, it is possible to obtain a SF with silk II conformation with a high content of water molecules, as well as a SF with silk I conformation that is completely insoluble in water, depending on the processing parameters.[23]

In SF films prepared from Ca^{2+}/FA solution Ca^{2+} ions can capture water from the atmosphere coordinating and trapping water molecules *via* the oxygen atoms.[14,24,25] Moreover, a previous study demonstrated that the conductivity of SF films at 25 °C with 57% RH was significantly increased when the mass ratio SF/Ca^{2+} was 70/30.[26]

The movements of ions in a fluid material (*e.g.* ionic liquids) are found to be responsible for a resistive switching behavior.[27,28] Actually, 2D-layered inorganic materials demonstrated excellent memory retention and uniformity in resistive switching.[28,29] Beyond this, the need to develop green electronic looks for biomaterials to design bio-memristive devices.[30–33] For these motivations, previous studies indicated that silk fibroin is a potential candidate for memory devices.[34,35] Both studies reported on the silk fibroin produced by standard protocol[36–38] based on lithium bromide (LiBr) dissolution of silk fibers and attributed the different states of the memristive switching phenomenon to oxidation and reduction of the SF.

In this study water soluble SF films containing Ca^{2+} ions were prepared by mixing degummed silk fibers and $CaCl_2$ in formic acid. Then, after the evaporation of the solvent, SF films were redissolved in phosphate-buffered saline (PBS) medium by varying the bath sonication time. The polymorphic nature of SF indicated that the silk I structure is the key secondary structure that promotes the dissolution of SF films in PBS for the regeneration of (i) water stable and elastic piezoelectric silk biomaterials with moderate β-sheet content, making them processable *via* EBP to obtain (ii) SF 3D biomaterials with resistive memory properties.

Materials and methods

Preparation of SF films

Silk cocoons were supplied by a local farm (Fimo srl, Milano, Italy) while indium tin oxide (ITO) slides, $CaCl_2$, FA and sodium bicarbonate ($NaHCO_3$) were supplied by Sigma-Aldrich. *Bombyx mori* cocoons were degummed in boiling aqueous $NaHCO_3$ solution (5 g in 200 ml of water) for 30 min. After rinsing, 0.70 g of silk fibers were dissolved in 5 ml of FA by adding $CaCl_2$ in weight ratio of 70/30 with respect to the silk amount. The SF solution was then sonicated in an ultrasound bath for 2 hours. SF films were produced by leaving the SF solutions to evaporate onto Petri dishes for 48 hours to remove any trace of the solvent. SF films were then redissolved in PBS 1× (pH 7.4) to get the same concentration of the FA solution and sonicated for 2 hours at room temperature in an ultrasonic bath. Finally, SF films were produced by leaving the SF solutions to evaporate onto Petri dishes for 12 hours.

To investigate the degradation SF/PBS films (circular shape with a diameter of 5 cm and thickness of 200 μm) were immersed at room temperature in 10 ml of phosphate-buffered saline (PBS) with a pH of 7.4. At a designated time, samples were washed with distilled water, dried in a desiccator, and weighed to estimate the weight variation.

Materials characterization

Mechanical characterization. Tensile tests of films were performed with a material testing machine Lloyd Instruments Mod. 30K with a transducer with a maximum load capacity of 5 N at a rate of 1 mm min^{-1} at room temperature. Stress–strain curves were recorded on rectangular-shaped samples (50 ± 0.5 mm, length 15 ± 0.5 mm and thickness of 0.5 ± 0.1 mm). For each film, three specimens were tested, and the results were averaged.

Infrared spectroscopy

Infrared spectra were recorded using a Fourier transform spectrometer from Jasco equipped with its diamond ATR (attenuated total reflection) module. The spectra were recorded in the 4000–400 cm^{-1} spectral range at a resolution of 2 cm^{-1}. Each measured spectrum was averaged from 300 scans. A background spectrum without sample was acquired using the same number of scans before each measurement. Spectral data were pre-processed by tracing a straight baseline from 1740 to 1560 cm^{-1}. To estimate the different components of amide I spectral profiles, a curve-fitting procedure was employed. Each component was assigned a Gaussian line shape, a full width at half height (FWHH) fixed at 20 cm^{-1}, and the weight was determined without constrains.

Raman spectroscopy

Raman spectroscopy was performed using an Olympus IX73 inverted confocal microscope coupled to the S&I MonoVista CRS+ spectrometer. Spot measurements on the samples were obtained using an excitation wavelength of 532 nm and a 50× objective lens (N.A. = 0.50). A grating of 300 grooves per mm and a slit aperture of 100 μm was chosen. Each spectrum was the average of 20 accumulations with an integration time of 7 s. The mean Raman spectra from spot measurements were calculated for comparison, after the baseline removal.

Circular dichroism

CD measurements were performed using a Jasco J810 spectropolarimeter in 1 mm path-length quartz cells. Spectra were collected in the range from 200 nm to 330 nm with a scan speed of 50 nm min^{-1}. All the CD profiles were acquired at room temperature. SF was measured in PBS at pH 4 and 7. The initial samples consisted of solutions of SF dissolved in PBS at pH 4, which were subsequently adjusted to pH 7.4 by adding NaOH. The initial solutions had a concentration of 3 mg ml^{-1}, and they were diluted to achieve a fibroin concentration of 0.6 mg ml^{-1}. Measurements were taken at 0, 1.5, and 3 hours after exposure to an ultrasonic bath. The two samples were also measured 2 months after solvation.

3D printing of SF solutions

Monolayer holey structures were 3D printed on the ITO slide using a custom-made piston-driven extrusion-based 3D printer.[21] Briefly, a 1.5 cm × 1.5 cm × 50 μm parallelepiped was

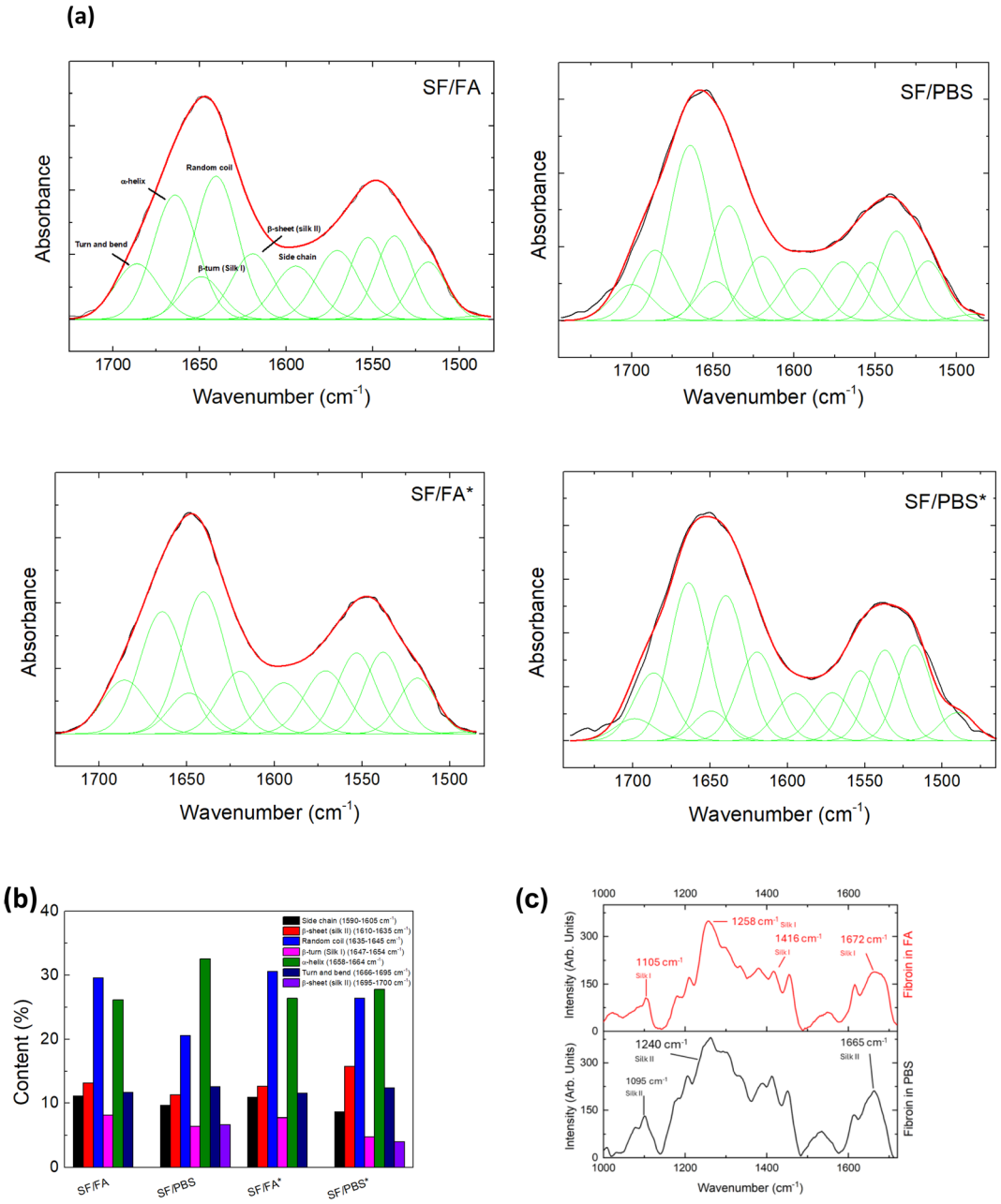

Fig. 1 (a) ATR-FTIR spectra (black line) and results of curve-fitting procedure (red and green lines) of SF films prepared by different processes and ultrasound treatment (the asterisks indicate the ultrasound treatment). (b) Relative weight of components obtained by curve-fitting procedure of ATR-FTIR spectra of SF films prepared by different processes and ultrasound treatment (the asterisks indicate the ultrasound treatment). The peak assignment of the amide I region in the 1610–1700 cm^{-1} range was done according to that reported by Lu *et al.*[23] Feature centered at frequencies out of this range were included to reproduce the amide I and II profile but were not considered to estimate the weight of the different protein conformations. (c) Raman spectra of SF films prepared from FA (red – upper panel) and PBS regenerated fibroin solutions (black – lower panel).

designed in Fusion360 and imported on Slic3r to obtain the structure gcode applying the following printing parameters: infill = 25%; print speed = 4 mm s^{-1}; volumetric flow = 0.17 mm^3 s^{-1}; needle diameter = 260 μm. Silk solutions were prepared as described above, and then sonicated in a bath (40 MHz, 30 °C) for two hours, before printing. After the printing process, the structures were dried at room temperature for 24 h, to allow the complete evaporation of the solvent.

To study the printability of the structure in term of shape retention, contact angle measurements were performed with the silk solution on the ITO-treated glass. Contact angle measurements on the SF/PBS film were performed at room temperature using an optical tensiometer, performing a sessile drop analysis (n = 15, drop volume = 2 μl).

Then, a morphological analysis of the holey structures was performed *via* optical imaging with a brightfield microscope (Leica DM 6M). Briefly, images of the grid lines were acquired, and their width was measured using the measurement tool of the microscope software (LASX). Then, a z-stack acquisition was performed (step dimension = 4 μm) and the line profile (*i.e.*, line thickness) was extracted by exploiting the Leica Map DCM software.

Fabrication and characterization of the piezoelectric and resistive memory devices

The fabrication of resistive memory involved SF 3D printed holey structures on ITO. A commercially available ITO coated glass substrate with a thickness of 80 nm and a sheet resistance of 30 Ω sq^{-1} was used as the bottom electrode. The SF from PBS solution was printed onto the substrate as reported above. Finally, an aluminum (Al) tape was employed as top electrode. The piezoelectric generator presented the SF from PBS solution as active layer. SF film was sandwiched between two electrodes composed of Al tape. The piezoelectric layer had a thickness of 150 μm. The open circuit voltage of the piezoelectric device as well as the *I–V* characterization of the resistive memory device were measured with a Keysight 4200A SCS source measurement unit. To investigate the conductivity properties of SF, an electric circuit consisting of LED (red color, at a forward voltage of 1.74 V), SF as a conductor and copper were connected in series and supplied with a DC power supply.

Statistical analysis

GraphPad Prism 9.2.0.332 (GraphPad software, San Diego, CA, USA) was used to assess the statistical significance of all comparison studies in this work. In the statistical analysis for comparison between multiple groups, a two-way ANOVA with Tukey's *post hoc* analysis (multiple comparisons) was conducted with the significance threshold of $*p < 0.05$, $**p < 0.01$, $***p < 0.001$ and $****p < 0.0001$.

Results and discussion

Structural changes in the silk films before and after the dissolution in PBS were analyzed by ATR-FTIR as reported in Fig. 1a.

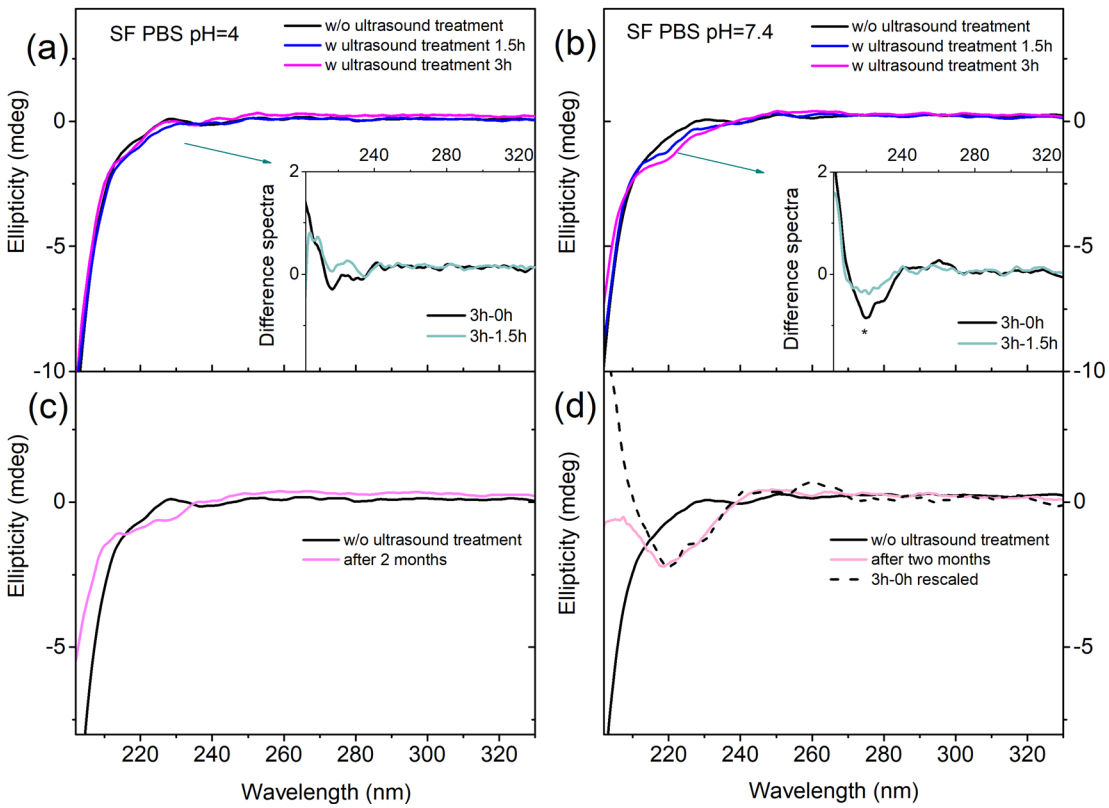

Fig. 2 CD spectra of SF in solution in PBS. On the top SF in buffer at pH 4 (a) and pH 7.4 (b) at different ultrasound treatments of the solutions (*e.g.* w/o ultrasound treatment, after 1.5 hours, and after 3 hours of ultrasound treatment). (c) SF in buffer pH 4 and (d) PBS pH 7.4 at the initial time and two months after solvation.

The secondary structure changes of SF protein were investigated by monitoring absorptions in the 1750–1450 cm^{-1} spectral region, and particularly the amide I (1700–1600 cm^{-1}) and amide II (1600–1500 cm^{-1}) bands. The peaks at ≈1622 cm^{-1} (amide I) and ≈1530 cm^{-1} (amide II) are characteristic of silk II secondary structure.[39] Silk I type II β-turns show a signature in the range 1647–1654 cm^{-1}. SF films showed also a peak at 1644 cm^{-1}, corresponding to random coil.[23]

SF films obtained from FA solution indicated a secondary hydrated silk I structure with the crystalline structure that can be controlled by changing the pH of the solvent.[40] After redissolving the SF films in PBS, the silk II structure is forming (Fig. 1a and b). This is substantiated by the observation of an additional peak in the amide I profile around 1695 cm^{-1}, which is indicative of antiparallel β-sheet conformations.[23] For the SF films prepared by ultrasound treatment, the total β-sheet content remains unaltered for the samples obtained from FA solution, but increases for those redissolved in PBS. In these samples, the β-turns silk I structures decrease (Fig. 1b), indicating the transition of an intermediate silk I structure to a silk II structure dominated by β-sheet antiparallel crystals.

The alterations in the secondary structure of SF protein were also monitored by Raman spectroscopy. Fig. 1c displays the Raman spectra of SF in the 900–1700 cm^{-1} range under acidic and neutral pH conditions. The position of the amide I band at 1672 cm^{-1}, amide III at 1258 cm^{-1} and C–C stretching at 1105 cm^{-1} observed for SF in FA are characteristic of silk I structure.[41] The red shift of these bands at 1665, 1240 and 1095 cm^{-1}, respectively, clearly suggest a different secondary structure for SF in PBS, with the prevalence of β-sheet conformation characteristic of silk II.[41]

To enhance our comprehension of the conformational changes taking place in the fibroin chains within the two distinct acidic/basic environments, we monitored the CD spectra of SF in solution under various conditions. Since SF is not entirely soluble in PBS, we employed two methods to facilitate its solubility: sonication and extended solvation time. Furthermore, because the strong absorbance of FA in the far-UV region saturates the CD spectrum, we replicated comparable acidic conditions by employing a buffer at pH 4. All experiments in the two different environments were conducted using the same procedures.

Fig. 2 shows the spectra of SF with and without ultrasound treatment at pH 4 and at pH 7.4, respectively. At the starting point, both spectra exhibit the characteristic shape of a random coil, with a minimum at approximately 200 nm, which in our spectra is only partly visible.[42] Upon analyzing the temporal evolution of spectral changes induced by ultrasound treatment, we observe that while sonication in buffer at pH 4 does not induce significant alterations (see Fig. 2a), a defined negative

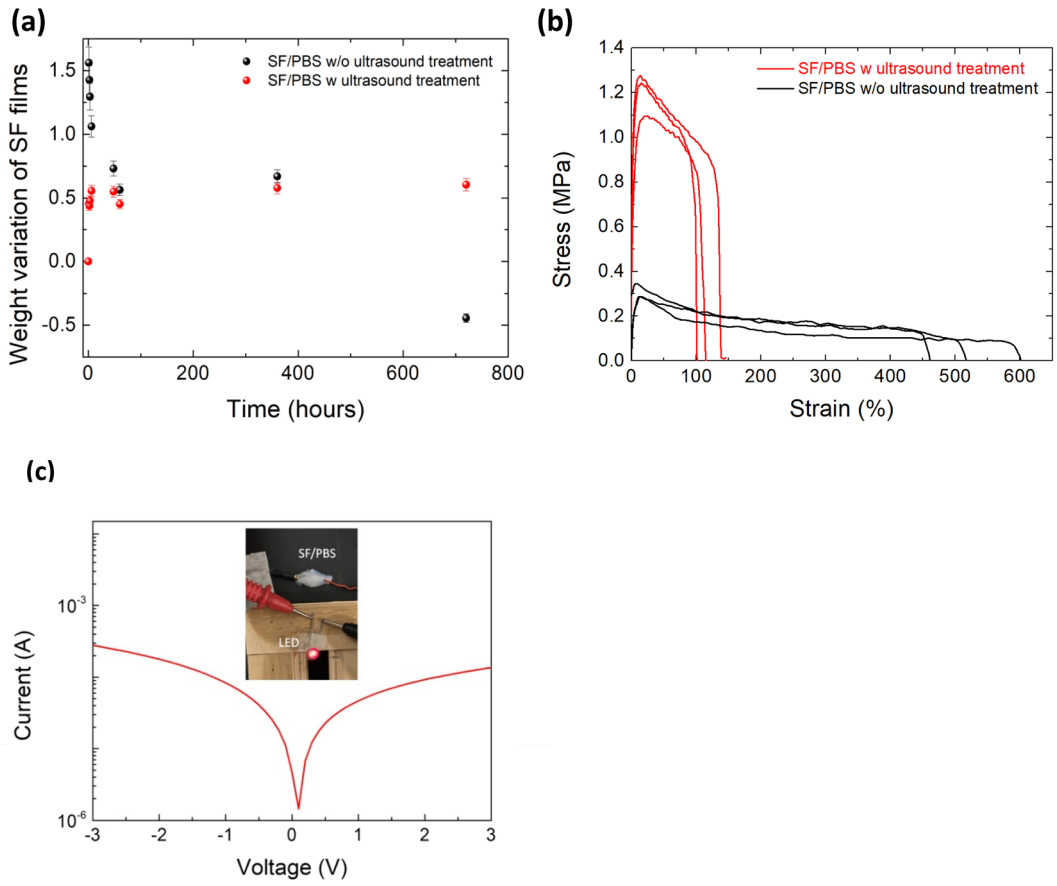

Fig. 3 (a) Weight variation and (b) representative tensile stress–strain curves of SF films prepared from PBS regenerated fibroin solutions w and w/o ultrasound treatment. (c) Demonstration of SF/PBS ionic conductor with DC applied to maintain current and illuminating LED.

band at 217 nm emerges in PBS at pH 7.4, suggesting the presence of some β-sheet structures (see Fig. 2b).[42]

We performed CD experiments also two months after solvation and found it quite interesting that there was no difference in the revealed conformation of SF at pH 4, which maintains a random coil structure (Fig. 2c). In contrast, in PBS at pH 7.4, the minimum characteristic of β-sheet is quite similar to the one induced by sonication (Fig. 2d). Our results suggest that using sonication or extending the solvation time allows a small fraction of the SF aggregates to become solvated in PBS at pH 7.4, and that the relevant conformation of the biomolecule in solution is silk II. On these grounds, we speculate that the formation of silk II in solution, under physiological conditions (*i.e.* pH 7.4), may be the early step in the formation of aggregate/crystalline structures. Interestingly, β-sheet formation and the subsequent gelation process were previously observed with CD at increasing pH,[43] albeit at SF concentrations two orders of magnitude higher than those used in the present experiment.

The presence of a moderate content of β-sheets is desirable to extend the utility of water-stable materials avoiding their mechanical embrittlement.[17,44,45] In this regard, the degradation of SF redissolved in PBS was measured after both processing conditions (*e.g.* w and w/o sonication) (Fig. 3a). Both groups showed an increase of the mass after a few hours of immersion being this effect more pronounced for the films w/o sonication. No difference in mass loss was then recorded between the two groups, but after 1 month the loss from the film obtained w/o sonication was higher than that from the film obtained after sonication (Fig. 3a). We then evaluated the mechanical properties of these films. Fig. 3b shows the stress–strain curve of the SF films redissolved in PBS. The results indicated that w/o sonication the film shows an elongation at break of 509 ± 69% that reduces to 98 ± 16% for the film deposited after ultrasound treatment showing an enhancement of the tensile strength from 0.30 ± 0.02 MPa to 1.19 ± 0.09 MPa. The effect of the ultrasound treatment on the reduced elongation at break and increased tensile strength of SF/PBS sample can be rationalized as follows: (1) the ultrasound helps a part of the non-crystalline region of SF chains to form a more ordered structure;[46] and (2) the ultrasound treatment distributes the calcium ions throughout the solution system enhancing the penetration into silk structure and promoting the formation of water molecules around the hydrated Ca^{2+} and increasing the distance between the silk chains.[47] The presence of hydrated Ca^{2+} gives ionic conductivity to the SF/PBS sample that was used as a conductor in a circuit to light a high-emitting diode (LED). As shown in Fig. 3c, SF/PBS ionic conductor was able to continuously transmit a steady DC electronic signal.

Previous studies have provided information about the origins of the piezoelectricity of silk. These results indicated that the piezoelectricity can be explained by the increasing content of β-sheets.[20,21] Moreover, the electrical properties of a resistive element can be tuned by 3D printing materials with predictable length and cross-sections.[48] For this motivation, we proceeded with the 3D printing of SF that maximizes silk II

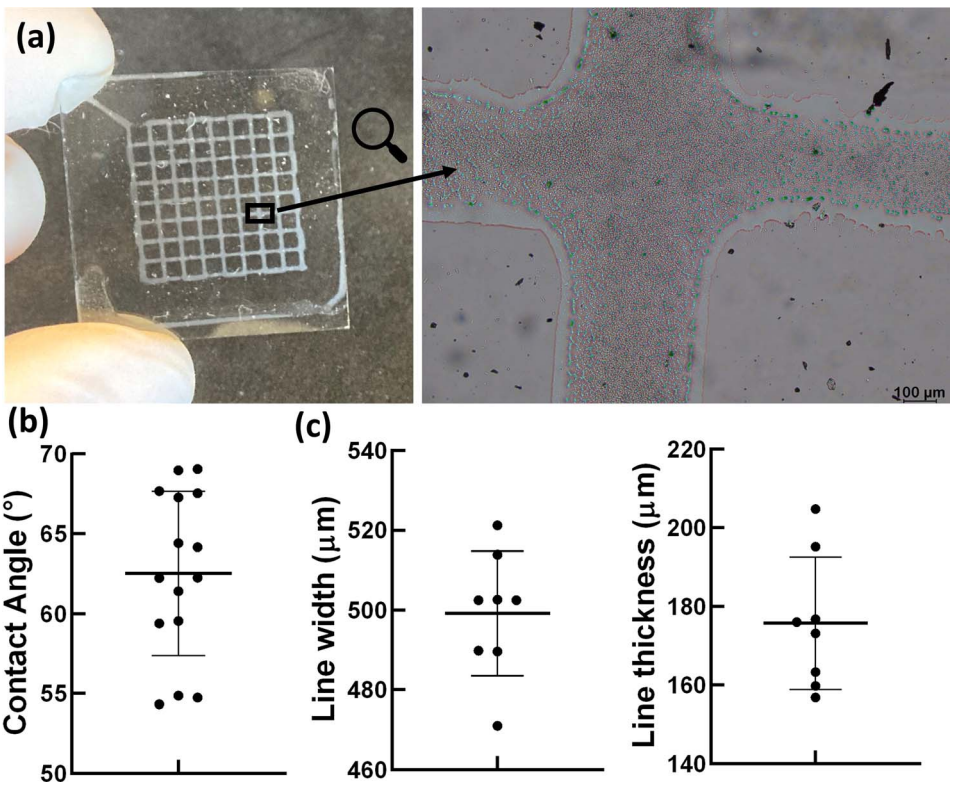

Fig. 4 (a) Optical image of the holey structures fabricated *via* extrusion-based 3D printing of SF solution in PBS on ITO, and a zoom-in image of the grid lines and intersection (scale bar = 100 μm). (b) Contact angle measurements. (c) Line width and thickness measurements of the printed holey structures.

crystallinity.[49] The silk-based solution under investigation proved to be easily extrudable by EBP and patterned in a grid-like structure (Fig. 4a). This is in accordance with the contact angle measurements that showed a contact angle between the silk solution and the ITO-treated glass around 62° (Fig. 4b). Indeed, as we previously showed in ref. 50, a high contact angle (up to 90°)[51] related to a lower wettability of the substrate by the printed solutions, reduces the lateral spreading of the printed line, and ultimately leads to a better printing accuracy. However, poorly wettable surfaces (contact angle higher than 90°) can lead to breaks of the printed line due a mechanism similar to the Plateau–Rayleigh instability.[52] Morphological analysis revealed a line width of 499 ± 15 μm, 2.5 times wider than the nozzle diameter, and a line thickness of 176 ± 16 μm, as reported in Fig. 4b.

It is well known that the function of the human brain depends on the synaptic plasticity between the presynaptic and the postsynaptic neuron.[53] Ca^{2+} ions are the prevalent

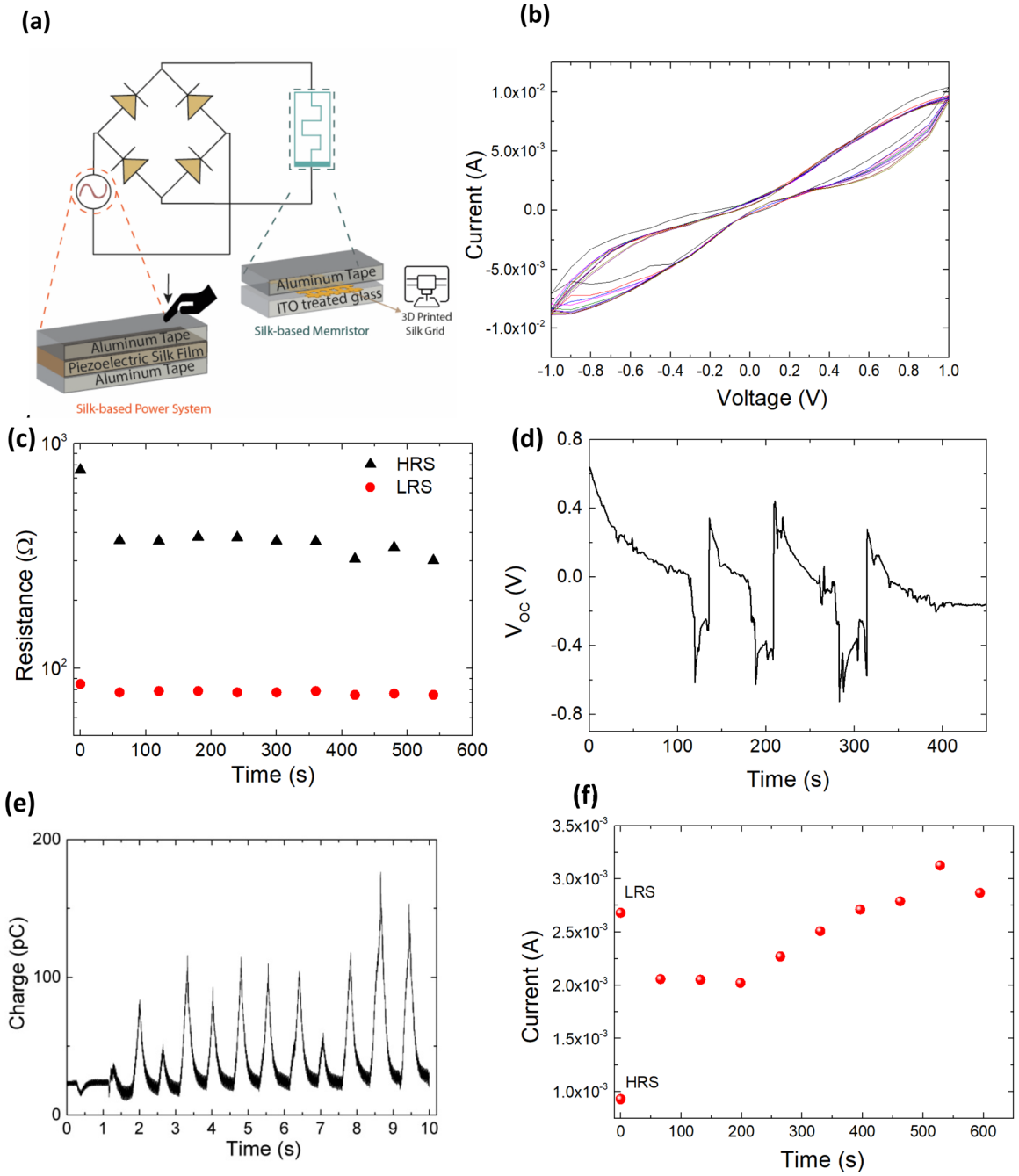

Fig. 5 (a) Schematic of SF memristor operated by SF generator. (b) *I*–*V* characteristics of 3D printed SF memristor. (c) Retention test of HRS and LRS of the SF holey structure under the application of a positive bias. The resistances were read at 0.3 V. (d) Open-circuit voltage (V_{OC}) and (e) current data recorded by SF film by applying and releasing a force of 0.1 N. (f) The short-time memory (STM) retention of the neuromorphic device based on SF 3D printed holey structure.

neurotransmitters that initiate the neuronal spikes, which control the synaptic plasticity.[54] A multistate memristive device can mimic this synaptic plasticity by applying repetitive pulses to observe gradual variations in the conductance state.[55]

Hence, ions movement can be directed in the presence of an external electric field and under negative and positive voltage sweep the current decreases due to ion metallization[55] as happens in the synapses (Fig. 5a). The measured current across the SF holey structure indicated that the conductivity decreases over time under ten voltage sweeps (Fig. 5b). This resistive switching behavior exhibits hysteresis in its current–voltage characteristics, similar to that was observed by Hota *et al.*[34] Initially, the device remains in its high resistance state, *i.e.* in 'OFF' state at a smaller bias. When the applied bias reaches a threshold of $\approx$+0.4 V, the device shows an increase in the current value, indicating that it is in its ON state (Fig. 5b). Similarly, at ≈ -0.2 V the device switches from a low resistance state (LRS) to high resistance state (HRS). The structural stability of the printed SF was assessed by microscopy and Raman analyses taken before and after voltage sweeps (Fig. S1†). By comparisons of the SF structure we did not observe changes with respect to the image reported in Fig. 2c and 4a, respectively. In Fig. 5c and S2† we report the memory retention performance of our SF-based memristor device at 0.3 V; even if the retention is low compared to other devices based on layered nanomaterials or metal oxides,[29] these results indicate the potentiality of SF for biomemristor devices and are comparable with those obtained by Hota *et al.*[34]

Therefore, the devices could reversibly be switched between HRS and LRS in DC sweep mode. For this motivation, we fabricated a piezoelectric device by inserting a SF film obtained from redissolution in PBS between two Al tape electrodes. Fig. 5d and e show the open-circuit voltage and current signal that was obtained by applying and releasing a force of 0.1 N at different time pulses. From this condition, we obtained an output voltage of $\geq$0.2 V and charge of 100 pC, and this output voltage is sufficient to supply the memristor. In addition, the open circuit voltage and the current of the SF piezoelectric film were reproducible and stable after continuously operating, as shown in Fig. 5d and e.

We applied ten pulses of 0.2 V produced by the SF generator to set the memristive device in a high resistance state (HRS), as shown in Fig. 5f. The switching transacts from LRS to HRS by applying a positive voltage sweep, and this phenomenon is similar to the operation of short-term depression (STD).[56,57] Then, we measured the conductivity of the proposed device by applying the 0.2 V pulse every 50 s. The current of the device started to increase after applying a pulse every 50 s. After 600 s, the device was set to the LRS condition. The device slowly transitioned from HRS to LRS; a phenomenon reminiscent of human memory devices.

Conclusions

In summary, SF films with a silk I structure can be redissolved in aqueous medium to obtain silk II films with β-sheet content that increases with increasing the ultrasonic treatment. The conformational transition of SF allowed the fabrication of water stable and elastic films used in designing a self-powered resistive memory device integrated with a silk-based piezoelectric generator. We have addressed the use of SF printable biomaterial with a silk II structure as a soft multistate resistive switching device. The switching transaction by applying input pulses to change the device state from LRS to HRS resembles short-term depression. By programming the secondary structure of natural proteins, we can pave the way for designing devices capable of detecting mechanical stimuli within the human body and storing data to provide feedback for medical treatments.

Author contributions

The manuscript was written with the contributions of all authors. All authors have approved the final version of the manuscript. V. L., R. M., M. A. C., I. C. and S. B. B. were involved in laboratory research; L. C., P. S., M. A. C., I. C., C. De M. and L. V. wrote the original draft; all the authors revised the original draft. L. V., L. C., A. P., C. De M. and P. S. contributed to the conceptualization of experiments and L. V. contributed to the overall coordination of the research activities and funding aquisition. All authors have read and agreed to the published version of the manuscript.

Conflicts of interest

There are no conflicts to declare.

Acknowledgements

This work has been funded by the European Union – NextGenerationEU under the Italian Ministry of University and Research (MUR) National Innovation Ecosystem grant ECS00000041 – VITALITY – CUP J97G22000170005 and CUP B43C22000470005. This study received funding from the European Union – Next-GenerationEU – National Recovery and Resilience Plan (NRRP) – Mission 4 Component 2, investment n. 1.1, Prin 2022 – Prometheus "4D printing self-deploying bio-enabled polymer scaffolds for the non-invasive treatment of bleeding intestinal ulcers", grant: 2022BZLTTK, CUP I53D23002200006. I. C. and C. D. M. acknowledge the support of the Crosslab Additive Manufacturing and the FoReLab of the Department of Information Engineering of the University of Pisa.

References

1 S. Cohen-Cory, *Science*, 2002, **298**, 770–776.
2 C. Yang and Z. Suo, *Nat. Rev. Mater.*, 2018, **3**, 125–142.
3 C. Keplinger, J. Sun, C. C. Foo, P. Rothemund, G. M. Whitesides and Z. Suo, *Science*, 2013, **341**, 984–987.
4 Z. Wang, T. Zeng, Y. Ren, Y. Lin, H. Xu, X. Zhao, Y. Liu and D. Ielmini, *Nat. Commun.*, 2020, **11**, 1510.

5 P. Yao, H. Wu, B. Gao, S. Burc Eryilmaz, X. Huang, W. Zhang, Q. Zhang, N. Deng, L. Shi, H.-S. Philip Wong and H. Qian, *Nat. Commun.*, 2017, **8**, 15199.
6 C. Wu, T. W. Kim, H. Y. Choi, D. B. Strukov and J. J. Yang, *Nat. Commun.*, 2017, **8**, 752.
7 J. Ryu, B. Kim, F. Hussain, M. Ismail, C. Mahata, T. Oh, M. Imran, K. K. Min, T. Kim, B. Yang, S. Cho, B. Park, Y. Kim and S. Kim, *IEEE Access*, 2020, **8**, 130678–130686.
8 M. U. Khan, G. Hassan, M. A. Raza, J. Bae and N. P. Kobayashi, *J. Mater. Sci.: Mater. Electron.*, 2019, **30**, 4607–4617.
9 H. Chun and T. D. Chung, *Annu. Rev. Anal. Chem.*, 2015, **8**, 441–462.
10 M. Onoda, *IEEJ Trans. Electr. Electron. Eng.*, 2020, **15**, 320–334.
11 G. Lauciricа, M. E. Toimil-Molares, C. Trautmann, W. Marmisoll and O. Azzaroni, *ACS Appl. Mater. Interfaces*, 2020, **12**, 28148–28157.
12 M. S. Mannoor, H. Tao, J. D. Clayton, A. Sengupta, D. L. Kaplan, R. R. Naik, N. Verma, F. G. Omenetto and M. C. McAlpine, *Nat. Commun.*, 2012, **3**, 763.
13 H. Tao, M. A. Brenckle, M. Yang, J. Zhang, M. Liu, S. M. Siebert, R. D. Averitt, M. S. Mannoor, M. C. McAlpine, J. A. Rogers, D. L. Kaplan and F. G. Omenetto, *Adv. Mater.*, 2012, **24**, 1067–1072.
14 A. K. Katz, J. P. Glusker, S. A. Beebe and C. W. Bock, *J. Am. Chem. Soc.*, 1996, **118**, 5752–5763.
15 Z. B. Cao, X. Chen, J. Yao, L. Huang and Z. Z. Shao, *Soft Matter*, 2007, **3**, 910–915.
16 H. J. Jin and D. L. Kaplan, *Nature*, 2003, **424**, 1057–1061.
17 S. Ling, Q. Zhang, D. L. Kaplan, F. Omenetto, M. J. Buehler and Z. Qin, *Lab Chip*, 2016, **16**, 2459–2466.
18 T. Yucel, P. Cebe and D. L. Kaplan, *Adv. Funct. Mater.*, 2011, **21**, 779–785.
19 S. Bittolo Bon, L. Valentini, M. Degli Esposti, D. Morselli, P. Fabbri, V. Palazzi, P. Mezzanotte and L. Roselli, *J. Appl. Polym. Sci.*, 2020, **138**, 49726.
20 S. Bittolo Bon, M. Rapi, R. Coletta, A. Morabito and L. Valentini, *Nanomaterials*, 2020, **10**, 179.
21 S. Bittolo Bon, I. Chiesa, M. Degli Esposti, D. Morselli, P. Fabbri, C. De Maria, A. Morabito, R. Coletta, M. Calamai, F. S. Pavone, R. Tonin, A. Morrone, G. Giorgi and L. Valentini, *ACS Appl. Mater. Interfaces*, 2021, **13**, 21007–21017.
22 S. K. Sohn, H. H. Strey and S. P. Gido, *Biomacromolecules*, 2004, **5**, 751–757.
23 Q. Lu, X. Hu, X. Wang, J. A. Kluge, S. Lu, P. Cebe and D. L. Kaplan, *Acta Biomater.*, 2010, **6**, 1380–1387.
24 J. Liu, Q. Chen, Q. Liu, B. Zhao, S. Ling, J. Yao, Z. Shao and X. Chen, *Adv. Mater. Technol.*, 2020, **5**, 2000430.
25 N. C. J. Strynadka and M. N. G. James, *Annu. Rev. Biochem.*, 1989, **58**, 951–998.
26 A. Ananthakrishnan, X. Du and M. G. Allen, *J. Phys. D Appl. Phys.*, 2021, **54**, 225104.
27 P. Zhang, M. Xia, F. Zhuge, Y. Zhou, Z. Wang, B. Dong, Y. Fu, K. Yang, Y. Li, Y. He, R. H. Scheicher and X. S. Miao, *Nano Lett.*, 2019, **19**, 4279–4286.
28 X. Yan, Q. Zhao, A. P. Chen, J. Zhao, Z. Zhou, J. Wang, H. Wang, L. Zhang, X. Li, Z. Xiao, K. Wang, C. Qin, G. Wang, Y. Pei, H. Li, D. Ren, J. Chen and Q. Liu, *Small*, 2019, **15**, 1901423.
29 A. C. Khot, T. D. Dongale, J. H. Park, A. V. Kesavan and T. G. Kim, *ACS Appl. Mater. Interfaces*, 2021, **13**, 5216–5227.
30 M. Ambrico, A. Cardone, T. Ligonzo, V. Augelli, P. F. Ambrico, S. Cicco, G. M. Farinola, M. Filannino, G. Perna and V. Capozzi, *Org. Electron.*, 2010, **11**, 1809–1814.
31 Y. C. Chang and Y. H. Wang, *Appl. Phys. Lett.*, 2015, **106**, 123302.
32 R. U. Sheth and H. H. Wang, *Nat. Rev. Genet.*, 2018, **19**, 718–732.
33 B. Sun, D. Liang, X. Li and P. Chen, *J. Mater. Sci.: Mater. Electron.*, 2016, **27**, 3957–3962.
34 M. K. Hota, M. K. Bera, B. Kundu, S. C. Kundu and C. K. Maiti, *Adv. Funct. Mater.*, 2012, **22**, 4493–4499.
35 J. Yong, B. Hassan, Y. Liang, K. Ganesan, R. Rajasekharan, R. Evans, G. Egan, O. Kavehei, J. Li, G. Chana, B. Nasr and E. Skafidas, *Sci. Rep.*, 2017, **7**, 14731.
36 S. Sofia, M. B. McCarthy, G. Gronowicz and D. L. Kaplan, *J. Biomed. Mater. Res.*, 2001, **54**, 139–148.
37 S. T. Parker, P. Domachuk, J. Amsden, J. Bressner, J. A. Lewis, D. L. Kaplan and F. G. Omenetto, *Adv. Mater.*, 2009, **21**, 1–5.
38 S. C. Kundu, B. C. Dash, R. Dash and D. L. Kaplan, *Prog. Polym. Sci.*, 2008, **33**, 998–1012.
39 X. Hu, D. L. Kaplan and P. Cebe, *Macromolecules*, 2006, **39**, 6161–6170.
40 B. D. Lawrence, F. Omenetto, K. Chui and D. L. Kaplan, *J. Mater. Sci.*, 2008, **43**, 6967–6985.
41 E. Pavoni, M. Tsukada and P. Taddei, *J. Raman Spectrosc.*, 2016, **47**, 1367–1374.
42 N. Greenfield, *Nat. Protoc.*, 2006, **1**, 2876–2890.
43 A. Matsumoto, J. Chen, A. L. Collette, U. Kim, G. H. Altman, P. Cebe and D. L. Kaplan, *J. Phys. Chem. B*, 2006, **110**, 21630–21638.
44 H.-J. Jin, J. Park, R. Valluzzi, P. Cebe and D. L. Kaplan, *Biomacromolecules*, 2004, **5**, 711–717.
45 H. J. Jin, J. Park, V. Karageorgiou, U. J. Kim, R. Valluzzi and P. Cebe, *Adv. Funct. Mater.*, 2005, **15**, 1241–1247.
46 Y. Xue, F. Wang, M. Torculas, S. Lofland and X. Hu, *ACS Biomater. Sci. Eng.*, 2019, **5**, 6361–6373.
47 X. Yu, Y. Hu, H. Shi, Z. Sun, J. Li, H. Liu, H. Lyu, J. Xia, J. Meng, X. Lu, J. Yeo, Q. Lu and C. Guo, *ACS Appl. Mater. Interfaces*, 2022, **14**, 48061–48071.
48 P. F. Flowers, C. Reyes, S. Ye, M. J. Kim and B. J. Wiley, *Addit. Manuf.*, 2017, **18**, 156–163.
49 X. G. Li, L. Y. Wu, M. R. Huang, H. L. Shao and X. C. Hu, *Biopolymers*, 2008, **89**, 497–505.
50 M. Alunni Cardinali, M. R. Ceccarini, I. Chiesa, S. Bittolo Bon, T. Rondini, M. Serrano-Ruiz, M. Caporali, S. Tacchi, A. Verdini, C. Petrillo, C. De Maria, T. Beccari, P. Sassi and L. Valentini, *ACS Omega*, 2024, **9**, 17977–17988.
51 A. Piqué and D. B. Chrisey, *Direct-Write Technologies for Rapid, Prototyping Applications: Sensors, Electronics, and Integrated Power Sources*, Academic Press, New York, 2001.

52 C. S. O'Bryan, T. Bhattacharjee, S. R. Niemi, S. Balachandar, N. Baldwin, S. T. Ellison, C. R. Taylor, W. G. Sawyer and T. E. Angelini, *3D Bioprinting of Organs*, 2017, vol. 42, pp. 571–577.
53 J. Ge, D. Li, C. Huang, X. Zhao, J. Qin, H. Liu, W. Ye, W. Xu, Z. Liu and S. Pan, *Nanoscale*, 2020, **12**, 720–730.
54 T. Y. Wang, J. L. Meng, M. Y. Rao, Z. Y. He, L. Chen, H. Zhu, Q. Q. Sun, S. J. Ding, W. Z. Bao, P. Zhou and D. W. Zhang, *Nano Lett.*, 2020, **20**, 4111–4120.
55 M. Y. Chougale, M. U. Kahn, J. Kim, R. A. Shaukat, Q. M. Saqib, S. R. Patil, T. D. Dongale, A. Bermak, B. Mohammad and J. Bae, *Adv. Eng. Mater.*, 2022, 2200314.
56 T. Wang, J. Meng, Z. He, L. Chen, H. Zhu, Q. Sun, S. Ding and D. W. Zhang, *Nanoscale Res. Lett.*, 2019, **14**, 102.
57 Z. Xu, F. Li, C. Wu, F. Ma, Y. Zheng, K. Yang, W. Chen, H. Hu, T. Guo and T. W. Kim, *NPG Asia Mater.*, 2019, **11**, 18.